Adiabatic potentials for Rydberg atoms in a ponderomotive optical lattice

Kelly Cooper Younge[1]**, Sarah Elizabeth Anderson and Georg Raithel**

FOCUS Center, Department of Physics, University of Michigan, Ann Arbor, MI 48109, USA
E-mail: kyounge@umich.edu

Abstract. We calculate the adiabatic potentials and adiabatic wavefunctions of Rydberg atoms in a one-dimensional ponderomotive optical lattice. All lattice-induced couplings between the degenerate high-angular-momentum Rydberg states are taken into account. To obtain insight into the underlying physics, we analyze the numerical results in terms of effective electric and magnetic fields produced by the lattice. Near the inflection points of the lattice potential and for sufficiently low principal quantum numbers ($n \lesssim 35$ in the cases studied), the adiabatic level structure resembles that of the dc Stark effect, and an effective electric-field model can be used to model the lattice-induced perturbation. Near the nodes and anti-nodes of the lattice field, the adiabatic level structure exhibits a combination of adjacent rotational and vibrational energy level sequences. Here, an analogy between the ponderomotive optical lattice and the diamagnetic problem works well to interpret the lattice-induced perturbation in terms of an effective magnetic field.

---

[1] Author to whom any correspondence should be addressed.

Contents

1. Introduction

Since the development of laser cooling and trapping of atoms in the 1980s, the idea that atoms can be organized and stored via the ac Stark shift produced by fields of interfering laser beams has been studied in numerous theoretical and experimental contexts [1]. The fact that the optical lattice potential can be modeled exactly and the lattice parameters can be controlled precisely via the laser beam geometry, intensity, frequency and polarization makes the optical lattice a very attractive system for a breadth of physics subfields. Recent studies include effects in condensed matter systems such as interacting fermions in periodic potentials (3D optical lattice) [2], purely quantum mechanical phenomena such as quantum random walks of atoms in a lattice [3], and the generation of entanglement for quantum information [4]. Adiabatic potentials for atoms in an optical lattice can be calculated semiclassically by treating the internal dynamics quantum mechanically along with a classical description of the center of mass motion. At each position in space, the atom–field interaction Hamiltonian is obtained and diagonalized, yielding position-dependent adiabatic energy eigenvalues. The adiabatic potential surfaces are generated by plotting the eigenvalues versus position.

Novel aspects arise when a Rydberg atom instead of a ground-state atom in an optical lattice is considered, because these atoms can have sizes on the order of the lattice period (as opposed to a ground-state atom that can be considered point-like in relation to the lattice period), and because the number of nearly degenerate states is much higher. We find that the lattice potential can be modeled by an effective electric field near the inflection points of the lattice, and an effective magnetic field near the nodes and anti-nodes. These effective fields lead to adiabatic potentials that resemble the dc Stark effect in the electric field case, and the diamagnetic problem in the magnetic field case. The similarity to the diamagnetic problem explains the observed rotational and vibrational energy level sequences visible in the adiabatic potentials. Our present work is in contrast with previous studies of ponderomotive optical lattices, where electric and magnetic fields were used to deliberately remove the degeneracy of the Rydberg states in order to eliminate the mixing between different states [5].

Confining Rydberg atoms in optical lattices has a number of potential applications [5]. The long coherence times and lifetimes of Rydberg atoms make them attractive candidates for quantum computing [6]–[8]. Ponderomotive optical lattices (named for the force on the quasi-free Rydberg electron) afford the possibility to create Rydberg atom traps that result in relatively small level shifts of the trapped atoms compared to other trapping methods [9]. This could be useful in precision spectroscopy experiments. Additionally, modulation of the optical lattice at microwave frequencies allows one to drive high-order multipole transitions between Rydberg levels with high spatial selectivity [10].

This paper is organized as follows. In section 2, we explain the origin of the ponderomotive shift and compare optical lattices for ground-state atoms and Rydberg atoms. In section 3, we describe the numerical methods used to calculate the potentials shown in this paper. We expand this discussion in the appendix. In section 4, we present and discuss the results, including how the adiabatic potential surfaces undergo a qualitative change as a function of principal quantum number, and how certain aspects of the behavior can be interpreted in terms of effective fields. We also provide several examples of adiabatic wavefunctions.

2. Rydberg atoms in a ponderomotive optical lattice

In the familiar case of ground-state atoms subjected to an optical lattice, adiabatic trapping potentials and wavefunctions result from an atom–field interaction that typically couples a few low-lying atomic states. In most cases, the excited states are adiabatically eliminated, and spatially periodic light-shift potentials are obtained for the ground-state levels [1]. Sometimes, state mixing due to lattice-induced Raman couplings between magnetic sublevels of the ground state occurs.

In the case of Rydberg atoms, the light shift is not as straightforward. While Rydberg levels are ground-state-like in that they have long lifetimes (typically $\sim 100\,\mu$s), lattice lasers applied to a Rydberg atom usually are not near-resonant with any optical transition, because transitions between Rydberg levels are in the GHz and THz frequency range. (For the purpose of this paper, we assume a generic case in which the lattice laser does not significantly couple the Rydberg level of interest down to a low-lying atomic level.) Following the methods used for ground-state atoms, one may obtain the light shifts and state mixing of Rydberg atoms in optical lattices by summing over the effects of virtual transitions to all available atomic states, as well as over all transitions through the continuum. A more practical method is based on the fact that the (optical) laser frequency is several orders of magnitude higher than the Kepler frequency of the Rydberg atom. Consequently, the effect of the laser field can be treated via a Born–Oppenheimer separation of variables, in which the dynamics at the optical frequency are accounted for by adding a Born–Oppenheimer potential to the equations that govern the dynamics in the slow degree(s) of freedom [5, 11]. The Born–Oppenheimer potential for the case of a (quasi-)free electron in a laser field is known as the ponderomotive potential, and it is equivalent to the time-averaged kinetic energy of the free electron in the oscillating electric field of the laser. The ponderomotive shift can be easily derived classically for a running wave where the electric field takes the form $\mathbf{E}(t) = \hat{x} E_0 \cos(\omega t)$. The electric field induces a driven oscillation of the electron, referred to as 'quiver' motion. The acceleration and velocity of the motion are given by

$$\ddot{x} = \frac{-eE_0}{m_{\mathrm{e}}} \cos(\omega t), \quad \dot{x} = \frac{-eE_0}{\omega m_{\mathrm{e}}} \sin(\omega t), \tag{1}$$

assuming that the initial velocity is zero. Here, $-e$ and m_e are the electron charge and mass, respectively. The time averaged kinetic energy is then

$$V = \frac{\omega}{2\pi} \int_0^{2\pi/\omega} \frac{1}{2} m_e \dot{x}^2 \mathrm{d}t = \frac{e^2 E_0^2}{4 m_e \omega^2}. \tag{2}$$

The same result for the ponderomotive potential can be found quantum-mechanically. Full quantum-mechanical expressions for the ponderomotive potential and the free-electron state in a laser field are provided by Friedrich [11] and references therein. This derivation for the ponderomotive potential is still applicable if the electric field varies slowly in space compared to the range of the electron's quiver motion. In the case of a one-dimensional optical lattice with beams counter-propagating in the z-direction, the electric field is given by

$$\begin{aligned}\mathbf{E}\left(\mathbf{r}, t\right) = E_x\left(z, t\right) \hat{x} &= E_{0x} \left[\cos\left(\omega t - kz\right) + \cos\left(\omega t + kz\right)\right] \hat{x} \\ &= 2 E_{0x} \cos\left(\omega t\right) \cos\left(kz\right) \hat{x}.\end{aligned} \tag{3}$$

For the cases of interest, optical lattices have spatial periods of the order of hundreds of nanometers, while the amplitude of the electron's quiver motion is of the order of a few picometers. Thus, the requirement that the electric field varies slowly in space is clearly satisfied, and equation (2) applies with $E_0 \rightarrow E_0(\mathbf{r})$ denoting the local amplitude of the optical electric field in the lattice. Consequently, we account for the lattice electric field by adding a position-dependent, sinusoidal perturbation potential to the Rydberg electron potential. The resultant gradient force pushes free electrons toward regions of lower laser field intensity. The ponderomotive force leads to well-known effects on above-threshold ionization [12] and Kapitza–Dirac scattering [13]. In the case where the electron is weakly bound in a Rydberg state, the ponderomotive shift added to the Rydberg level has been studied in [14, 15] and, for instance, gives rise to observable structures in above-threshold ionization [16, 17].

Besides the fact that the origin of the light shifts of ground-state and Rydberg atoms is fundamentally different, there are additional differences between these two cases. Since the size of Rydberg atoms is of the order of the lattice period, Rydberg atoms sample an entire region of the lattice at once, whereas ground-state atoms are usually considered point-like particles in relation to the lattice period. The ratio between Rydberg-atom size and lattice period can be tuned over a wide range around unity via the principal and the magnetic quantum numbers. Further, the number of states being coupled by the lattice field is much larger for Rydberg atoms than it is for ground-state atoms. The adiabatic wavefunctions of the Rydberg electron in ponderomotive optical lattices typically are coherent superpositions of tens to hundreds of states. Also, these wave functions vary as a function of the center-of-mass coordinate of the atom in the lattice. This is in contrast to the case of ground-state atoms in an optical lattice, in which the adiabatic wavefunctions are spatially varying spin states.

3. Numerical methods

The adiabatic potential surfaces shown in this paper are calculated by adiabatically eliminating the electron quiver motion from the center-of-mass motion of the atom via the Born–Oppenheimer approximation along the lines of [5]. The result of this elimination is that an optical standing wave of the type of equation (3) adds a ponderomotive lattice potential

$$V_{\mathrm{P}} = \tfrac{1}{2} V_0 \left(1 + \cos\left(2k\left(z + z_0\right)\right)\right) \tag{4}$$
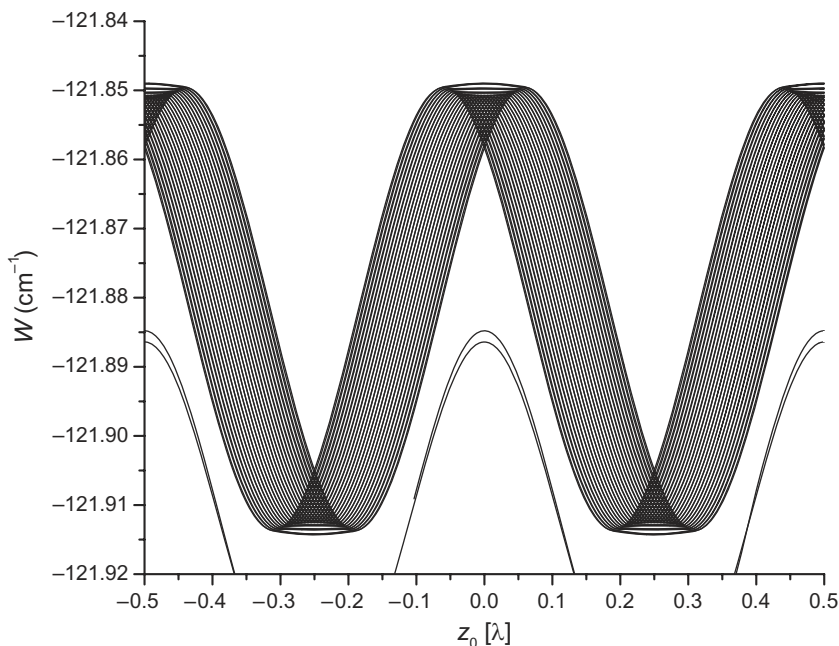
Figure 1. Adiabatic potentials in wavenumbers, W, for an optical lattice with $V_0 = 2\,\text{GHz}$, $n = 30$ and $m_j = 2.5$. These potentials exhibit distinct regions of approximately linear and quadratic behavior, explained in the text.

to the inner-atomic Coulomb potential. Here, $V_0 = \frac{e^2 E_0^2}{m_e \omega^2}$ with single-beam electric field E_0, z_0 is the atomic center-of-mass coordinate, and z is the relative (internal) coordinate of the Rydberg electron. The full atomic Hamiltonian, in atomic units, is then

$$H = \frac{p^2}{2} - \frac{1}{r} + V_c(r) + V_P(z + z_0) + V_{LS}, \tag{5}$$

where $V_c(r)$ is a short-range core potential accounted for by using the proper quantum defects of the atom and V_{LS} is the fine structure. The variable z_0 is a classical parameter of the Hamiltonian (not an operator). We find the eigenvalues and eigenfunctions of this Hamiltonian using an expansion method explained in detail in the appendix. The results of our calculations are presented in the following section.

4. Results

4.1. Overview

In accordance with ongoing experimental efforts, in our calculations we have used the quantum defects of rubidium and a lattice laser wavelength of 1064 nm. Figure 1 shows the adiabatic potentials versus the center-of-mass atomic position, z_0, for the hydrogenic states of $n = 30$, $m_j = 2.5$ with a lattice depth $V_0 = 2\,\text{GHz}$. To achieve a lattice depth of 2 GHz experimentally, one would need a laser intensity of about $20\,\text{MW}\,\text{cm}^{-2}$, which could be achieved by focusing a 5 W beam into a spot of about $5\,\mu\text{m}$. Figures 2 and 3(a) show the corresponding potentials for $n = 45$ and 65. The value of $m_j = 2.5$ is chosen for the simulation because it corresponds to the
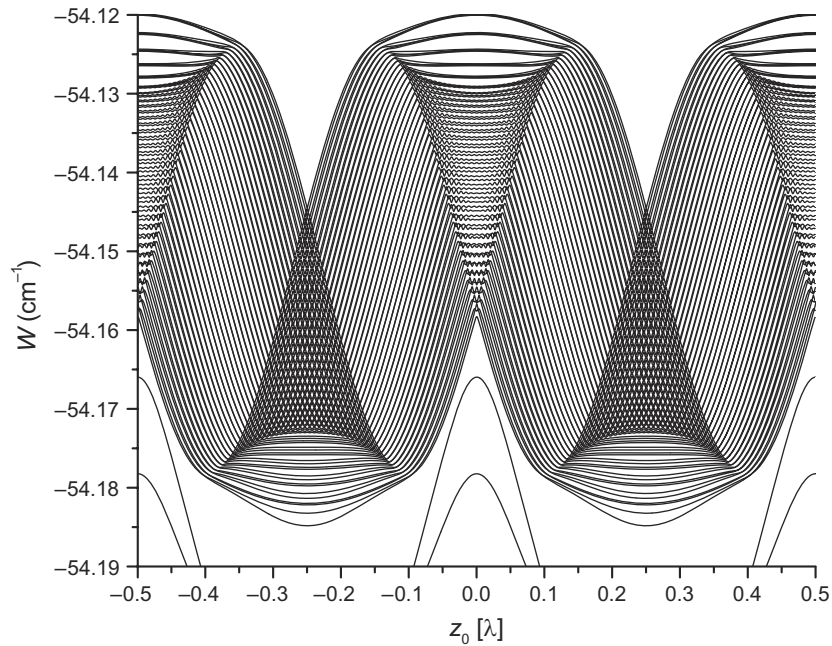
Figure 2. Adiabatic potentials for an optical lattice with $V_0 = 2$ GHz, $n = 45$ and $m_j = 2.5$. The linear region over which the lattice perturbation can be modeled as an effective electric field is much narrower than that for $n = 30$ (see figure 1).
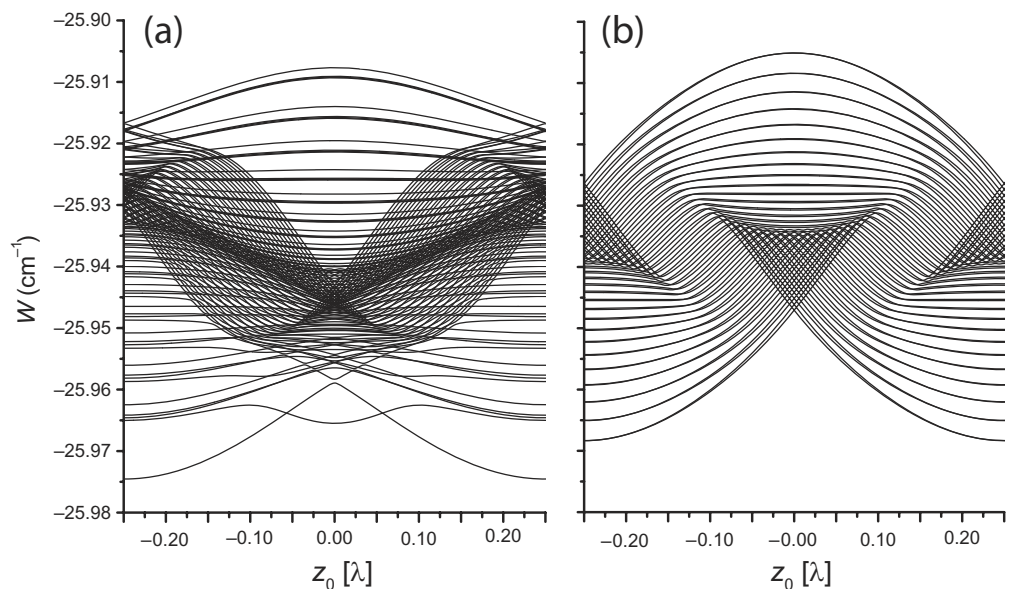

Figure 3. Adiabatic potentials for an optical lattice with $V_0 = 2$ GHz, $n = 65$ and $m_j = 2.5$ (panel (a)) and $m_j = 32.5$ (panel (b)). For $m_j = 2.5$, because of the extent of the Rydberg atom wavefunction, there are no longer clear distinctions between different regions of the lattice, as the wavefunction of the Rydberg atom averages over many parts of the potential. For $m_j = 32.5$, the number of states is reduced and the linear- and quadratic-like regions reemerge (see text).

state that would be reached when exciting out of a $P_{3/2}$ state and using σ^+ optical pumping. The anti-nodes of the optical lattice occur at $0, \pm\lambda/2, \pm\lambda, \ldots$ and the nodes at $\pm\lambda/4, \pm3\lambda/4, \ldots$.

Since in all the cases studied in this paper the lattice depth is much less than the Kepler frequency, lattice-induced state mixing only extends over states of similar effective quantum numbers. Hence, the lattice potential primarily mixes the levels with zero quantum defect (for rubidium these are all levels with angular momentum $l \geqslant 5$). With increasing ratio of lattice depth to the Kepler frequency, the G and F-levels may mix with the hydrogenic levels as well.

For Rydberg states with principal quantum numbers $n \lesssim 35$, the adiabatic potentials exhibit a simple structure resembling a set of interlaced sine-like curves that are all quite similar to the underlying free-electron ponderomotive potential, equation (4). This behavior can be readily explained as follows. Each of the adiabatic states that correspond to potentials shown in figure 1 is a superposition of many Rydberg states. All the components of the superposition states have sizes less than a lattice period and, hence, the sizes of the adiabatic state wavefunctions are also less than a lattice period. As a consequence, all adiabatic states experience a shift that approximately equals the free-electron ponderomotive potential evaluated at the center-of-mass location of the atom, which corresponds to setting $z = 0$ in equation (4).

Considering the detailed behavior of the adiabatic potentials in figure 1, one notes several qualitatively different regions. Between the nodes and anti-nodes, most adiabatic potentials are approximately straight, non-intersecting curves. In these regions, the lattice perturbation can be modeled via an effective electric field, as discussed in section 4.2 below. Near the nodes (anti-nodes) of V_P, we find regions of intersecting potentials and, below (above) in energy, regions of nearly flat, non-intersecting potential curves with non-uniform energy separations. In these regions, the lattice-induced perturbation is quadratic and can be modeled via an effective magnetic field, as discussed further in sections 4.3 and 4.4.

With increasing principal quantum number, the atomic diameter (of order $2n^2$ to $4n^2$) approaches and eventually exceeds the lattice period, and the number of levels that substantially mix increases. As a result, as n increases the sets of adiabatic potentials appear more widely spread out (figure 2), and eventually form convoluted patterns (figure 3). This behavior reflects the fact that once the wavefunction of the atom extends over a significant part of the lattice period (532 nm), the effective electric and magnetic field models are no longer applicable.

It is noted that the sets of adiabatic potentials near the anti-nodes and the nodes ($z_0 = 0$ versus $z_0 = \pm\lambda/4$) are not exactly symmetric to each other under the transformation $z_0 \rightarrow z_0 \pm 0.25\lambda$ and $W \rightarrow -W + \text{const}$. The asymmetry is most easily seen for higher n-values, such as in figures 2 and 3(a). The deviation from perfect symmetry is due to the quantum defects, which lead to an asymmetric placement of several unperturbed low-angular-momentum levels (S, P, D, F and G) about the hydrogenic manifolds.

In figures 1 and 2, there are two adiabatic potentials that are slightly offset toward lower energy from the main manifold and that exhibit a fairly simple spatial dependence. These potentials correspond, respectively, to the 30G and 45G Rydberg states that have a quantum defect of 0.00405 [18]. In figures 1 and 2, the adiabatic potentials for the G-levels are less complex than those seen for the bulk of quantum-defect-free levels because the G-levels are sufficiently non-degenerate from the quantum-defect-free levels that minimal lattice-induced state-mixing occurs. In both figures, there are two adiabatic potentials for the G-state, because the $m_j = 2.5$ manifold contains both $|n, l = 4, m_l = 2, m_s = 1/2\rangle$ and $|n, l = 4, m_l = 3, m_s = -1/2\rangle$ components, with $n = 30$ and 45, respectively. As the fine structure coupling of the G-components is very small, they do not mix and exhibit slightly different lattice-induced shifts.

Hence, the adiabatic potentials at the bottom of figures 1 and 2 correspond to adiabatic electronic states that are approximately given by $|n, l = 4, m_l = 2\rangle$ and $|n, l = 4, m_l = 3\rangle$. In figure 3, the lattice-induced coupling is strong enough that the G-levels are mixed into the manifold of quantum-defect-free levels.

Further qualitative changes are observed when varying m_j while keeping n fixed. In figure 3, we compare the adiabatic potentials for $n = 65$ and $m_j = 2.5$ (panel (a)) and $m_j = 32.5$ (panel (b)). As m_j is increased, the quantum states generally become more pancake-like and extend over a smaller range of z. As a result, the larger the value of m_j, the higher the value of n up to which the ponderomotive lattice can be modeled using effective electric and magnetic fields. This is because the effective-fields model gradually loses validity as the extension of the quantum states in the z-direction approaches the lattice period. For instance, figure 3(b) clearly breaks up into a region resembling the Stark effect and a region resembling a diamagnetic spectrum, while figure 3(a) is much more complex and no such analogy can be made. It is also noted that in the case of figure 3(b) all states in the manifold are quantum-defect-free, and the adiabatic potentials exhibit perfect symmetry under the transformation $z_0 \rightarrow z_0 \pm 0.25\lambda$ and $W \rightarrow -W + \text{const}$.

4.2. Effective electric field

For atomic center-of-mass positions, z_0, near the inflection points of the ponderomotive potential, equation (4), and for Rydberg-atom wavefunctions with sufficiently small extension in the z-direction, the potential can be modeled using an effective electric field. The maximum gradient (and thus maximum force) occurs at the inflection points of equation (4) and has a value of $V_0 k$, corresponding to an effective electric field of $F = V_0 k/e$. For a lattice depth of 2 GHz, the effective electric field at the inflection point is $F = 0.49 \, \text{V cm}^{-1}$. Using this value, the spacing between the adiabatic potential curves near the lattice inflection points can be predicted for all n via $\Delta W = 3nF$ (in atomic units). Figure 4 shows the predicted values of ΔW using this effective electric field model, along with the actual spacing between the adiabatic potential lines for a range of n and $m_j = 2.5$ (blue triangles) and $m_j = n - 2.5$ (red squares). For $m_j = 2.5$, the effective electric field model predicts ΔW well up to $n \approx 37$. For higher n, the values for ΔW become relatively constant, and then start to decrease around $n = 50$. This behavior is attributed to the fact that with increasing n the wavefunctions of Rydberg atoms located at an inflection point increasingly extend into regions of decreasing potential gradient, i.e. smaller effective electric fields.

The n-value up to which the effective electric field model holds increases with m_j, because with increasing m_j the wavefunctions become more and more concentrated in the plane transverse to the lattice quantization axis (the xy-plane). For the case $m_j = n - 2.5$ shown in figure 4, only a few near-circular Rydberg states are present in the calculation. Since these states mostly extend in the xy-plane, they do not average over the lattice potential as much as the lower-m_j states. The red squares in figure 4 show that for $m_j = n - 2.5$, the model of an effective electric field remains valid over a much larger n-range than for low m_j. As a minor aside, it is noted that for large m_j there is no fine structure coupling. As a result, the computation of adiabatic potentials for m_j yields two decoupled manifolds of states, namely one with $m_l = m_j - 1/2, m_s = 1/2$ and another with $m_l = m_j + 1/2, m_s = -1/2$. Looking at both manifolds combined in one plot, the adiabatic levels are interlaced in a way that the apparent level spacing equals $(3/2)nF$. In contrast, at low values of m_j, the adiabatic potentials are
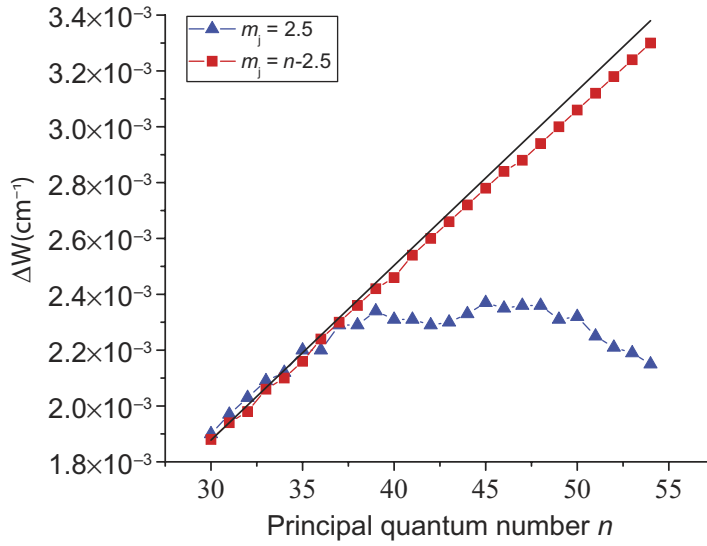
Figure 4. Splitting between adjacent adiabatic potential lines at the inflection point of the lattice for $m_j = 2.5$ (blue triangles) and $m_j = n - 2.5$ (red squares). The splitting values for $m_j = n - 2.5$ are multiplied by a factor of two (see text). The solid line shows the splitting predicted by the effective electric field model.

grouped in pairs of two with a pair-to-pair spacing of $3nF$ (see figures 1 and 2 near $z_0 = \pm\lambda/8$). To compare the cases $m_j = 2.5$ and $m_j = n - 2.5$ in figure 4, we multiply the spacing observed for the case $m_j = n - 2.5$ by a factor of two.

The n-range over which the effective electric field model is applicable can be estimated for low-angular-momentum states (blue triangles in figure 4) using the condition that the diameter of the atom must be less than half the lattice period, $4n^2 < \lambda/4$. This yields $n < 35$, which agrees well with what is seen in figure 4. For near-circular states (red squares), we estimate, based on the scaling behavior of radial and angular wavefunctions, that the effective electric field model should be valid up to $n \sim 250$.

4.3. Effective magnetic field

Figure 5 shows a zoomed-in part of the spectra depicted in figure 1 centered around the anti-node of the lattice at $z_0 = 0$. The highest energy levels resemble those that would be obtained for a rigid rotator (energy level spacings progressively increasing), while the bottom of the spectra looks more like the energy levels of a harmonic oscillator (fixed energy level spacings). This phenomenology is very similar to that found for Rydberg atoms in a magnetic field in the l-mixing regime, i.e. a regime in which the magnetic field is strong enough that the l-states of a given n-manifold become mixed. The term responsible for the l-mixing is the diamagnetic interaction: $\frac{1}{8}B^2r^2\sin^2\theta$ in atomic units. Here, we use spherical coordinates (r, θ, ϕ), and the lattice axis, z, corresponds to $\theta = 0$. In the following, we show that there is indeed a close similarity between the diamagnetism of Rydberg atoms in the l-mixing regime and the adiabatic spectra observed near the maxima and minima of ponderomotive optical lattices.

To establish the relationship between the diamagnetic perturbation and the ponderomotive optical lattice, we consider the lattice-induced perturbation of the Rydberg electron potential
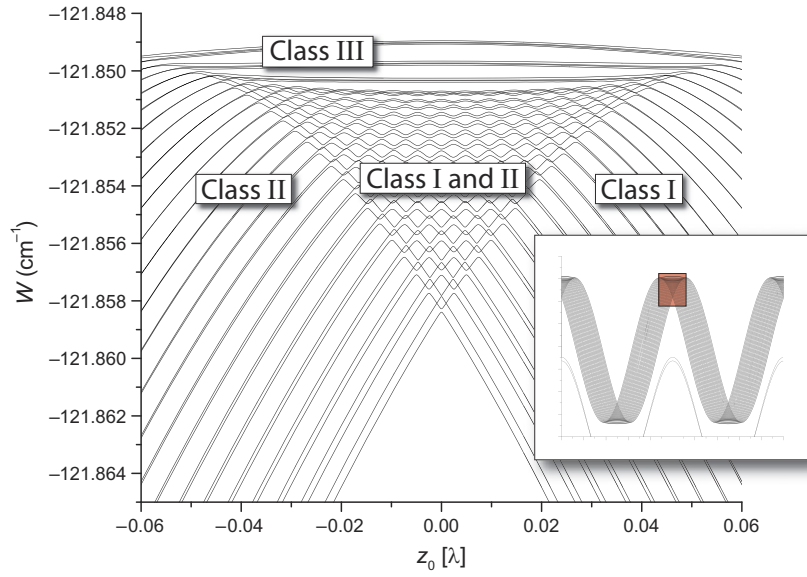
Figure 5. A closer look at the adiabatic potential for a $V_0 = 2\,\text{GHz}$ lattice with $n = 30$ and $m_j = 2.5$ reveals three classes of states. Class I consists of vibrational states with a positive dipole moment, class II consists of vibrational states with a negative dipole moment, and class III consists of rotational states.

for an atom with center-of-mass position located at a maximum of the standing-wave light field ($z_0 = 0, \pm\lambda/2, \pm\lambda, \ldots$):

$$V = \tfrac{1}{2} V_0 \left(1 + \cos 2kz\right). \tag{6}$$

This potential can be approximated up to second order, yielding a harmonic approximation of the perturbation that is valid for Rydberg atoms with wavefunctions much smaller than the lattice period:

$$V \approx V_0 - \frac{4\pi^2 V_0}{\lambda^2} r^2 + \frac{4\pi^2 V_0}{\lambda^2} r^2 \sin^2 \theta. \tag{7}$$

This expression shares the $r^2 \sin^2 \theta$-term with the diamagnetic perturbation, has an irrelevant constant, V_0, and includes a term $\propto -r^2$. The $r^2 \sin^2 \theta$-term of the lattice-induced perturbation leads to the striking similarities between diamagnetic spectra and adiabatic energy levels of Rydberg atoms near the maxima of ponderomotive lattices. The term $\propto -r^2$ is only present in the ponderomotive-lattice case; it is, obviously, responsible for some quantitative differences observed between the diamagnetic case and the ponderomotive-lattice case. Comparing the respective pre-factors of the $r^2 \sin^2 \theta$-term and using $V_0 = e^2 E_0^2 / (m_e \omega^2)$, we find that the ponderomotive potential for a Rydberg atom situated at a lattice maximum corresponds to an effective magnetic field of

$$B = \frac{2\sqrt{2} E_0}{c}, \tag{8}$$

where E_0 is the electric-field amplitude of a single laser beam forming the ponderomotive lattice. Similarly, for Rydberg atoms located at the nodes ($z_0 = \pm\lambda/4, \ldots$) the lattice-induced
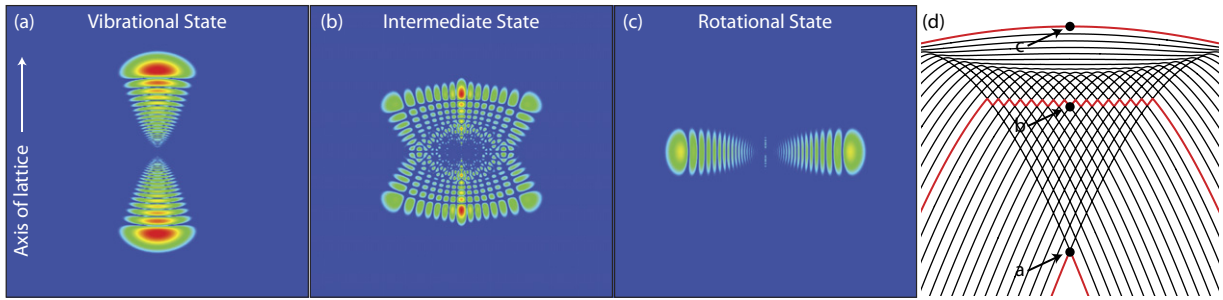
Figure 6. Wavefunction amplitude squared for an $n = 30$ atom at $z_0 = 0$ for three different states, and the corresponding set of adiabatic potentials. Wavefunctions and potentials are calculated without fine structure or quantum defects. (a) The lowest-energy adiabatic potential is a state that is purely vibrational and thus extends along the axis of the lattice. (b) The wavefunctions for higher energies compared to that shown in (a) gain more excitation transverse to the axis of the lattice. (c) The highest-energy adiabatic potential corresponds to a state that is purely rotational, extending in the plane transverse to the lattice axis. (d) Adiabatic potentials near $z_0 = 0$. The black dots identify the energies and locations for which the wavefunctions are calculated.

perturbation of the Rydberg electron potential is

$$V \approx \frac{4\pi^2 V_0}{\lambda^2} r^2 - \frac{4\pi^2 V_0}{\lambda^2} r^2 \sin^2 \theta. \tag{9}$$

Aside from an additive constant V_0, this is the negative of equation (7). This symmetry is the reason for the (approximate) symmetry of the adiabatic lattice potentials under the transformation $z_0 \to z_0 \pm 0.25\lambda$ and $W \to -W + \text{const}$.

The effect of the diamagnetic perturbation has been studied in great detail [19]–[22]. In these papers, it has been established and explained why the diamagnetic perturbation leads to adjacent rotor-like and vibrator-like energy level sequences; these are very similar to the level sequences seen at $z_0 = 0$ in figure 5 and in several other figures in this paper. The rotor-like and vibrator-like energy level sequences have a noteworthy explanation based on classical mechanics. Classically, in both the diamagnetic problem and in ponderomotive lattices (for atoms situated at $z_0 = 0$ and not too large in size), there exist two types of precession patterns of perturbed Kepler orbits [20]. In one type, the electron orbit remains mostly aligned with the magnetic-field axis or the lattice-beam direction with the semi-major axis precessing about that direction. This type of precession behavior corresponds to the vibrational states in the spectrum, found on the lower-energy side of the manifold. In the other type, the electron orbit remains mostly aligned in the plane transverse to the magnetic field (or the lattice-beam direction), and the semi-major axis periodically precesses through that plane. This type of precession behavior corresponds to the rotational states in the spectrum, found on the high-energy side of the manifold.

The electronic wavefunctions of Rydberg states at $z_0 = 0$ closely reflect the probability distributions that follow from the above described classical dynamics. In figure 6, the squares of the magnitudes of the wavefunctions for three different states are shown. To simplify the discussion, the wavefunctions are calculated for an optical lattice without fine structure or quantum defects. In each case, the atom is located at position $z_0 = 0$. The wavefunctions are

cylindrically symmetric about the axis of the lattice. Panel (a) shows the fundamental vibrational state. This is the lowest-energy state, and its wavefunction extends along the axis of the lattice. Panel (b) shows an intermediate state. Compared to the lowest-energy vibrational state, this intermediate state has some excitation transverse to the lattice, and it has a rather complex node-line structure. Panel (c) shows the highest energy state. This state extends entirely in the plane transverse to the lattice and thus is purely rotational. For reference, panel (d) shows the adiabatic potentials for all of the $n = 30$ states. The states corresponding to the wavefunctions in panels (a)–(c) are labeled.

It is noted that the wavefunction squares of vibrational states located at $z_0 = 0$ have two symmetric lobes, one pointing along $+z$ and the other along $-z$. The wavefunction amplitude of the state displayed in figure 6(a) is symmetric under z-inversion. There exists another, practically degenerate vibrational state that is anti-symmetric under z-inversion and whose energy exceeds the energy of the symmetric state only by a minute amount. This behavior reflects the fact that the underlying classical system has two degenerate vibrational electron orbits, one extending along positive and the other along negative z. The analogous quantum system exhibits near-degenerate, symmetric and anti-symmetric wavefunctions with lobes pointing along the $+z$ and $-z$ directions. In fact, a close study of figure 6(d) reveals that all vibrational states come in pairs of almost degenerate states; these pairs are near-identical states, one of which is symmetric and the other is anti-symmetric under z-inversion. An inspection of figure 6(d) also shows that the near-degeneracy is lifted as soon as z_0 deviates from $z_0 = 0$. The rotational states do not exhibit this near-degeneracy.

4.4. Parallel effective electric and magnetic fields

We finally consider the case of atoms located in the vicinity of $z_0 = 0$, at a distance less than approximately $\lambda/8$. As discussed in the previous chapter, the curvature of the ponderomotive potential generates a quantum behavior similar to that found in an equivalent magnetic field. In addition, in section 4.2 it has been established that a linear component of the ponderomotive potential can be modeled via an equivalent electric field. Hence, one may expect that for $z_0 \lesssim \lambda/8$ Rydberg atoms in ponderomotive lattices can be modeled using effective parallel electric and magnetic fields, with a fixed effective magnetic field $B = 2\sqrt{2}E_0/c$ and an effective electric field given by $F \approx -2V_0 k^2 z_0/e$. We thus expect a situation similar to that in [22], where helium Rydberg states in parallel electric and magnetic fields were studied. It has been pointed out in a number of studies that this type of system leads to three classes of states, referred to as I, II and III [21, 23, 24]. Classes I and II are vibrational states with a positive or negative electric dipole moment along the z-axis, respectively. States in class III are rotational states. The ratio of the electric and magnetic fields determines the classes of states that are available. In the present context, in the plots of adiabatic potentials of sufficiently small Rydberg states, the z_0-axis is analogous to an electric-field-scale, as the effective electric field $E \approx -2V_0 k^2 z_0/e$. Plotting the adiabatic potentials for $|z_0| \lesssim \lambda/8$, we indeed observe a striking similarity between the potential surfaces of Rydberg atoms in a ponderomotive lattice and the spectra of Rydberg atoms in parallel electric and magnetic fields. This is seen when comparing figure 5 and corresponding figures in the above references, in particular the first figure in [22].

As can be seen in figure 5, as the ratio of the effective electric and magnetic fields (linear to quadratic perturbations) increases, i.e. when moving from $z_0 = 0$ to $\lambda/8$, all states turn into class I states. The situation is similar when moving from $z_0 = 0$ to $-\lambda/8$, except that the effective electric field now points in the opposite direction, and all states turn into class II states.

A close look at the first figure in [22] and figure 5 reveals several fine differences, including an upward curvature of the class III states and a lack of curvature in the class I/II states in [22]. These differences are attributed to the inhomogeneity of the effective electric field in the lattice and to the presence of the term $-\frac{4\pi^2 V_0}{\lambda^2} r^2$ in the lattice-induced Hamiltonian. Nonetheless, in comparison with these differences, the overall similarity between the first figure in [22] and figure 5 is compelling.

5. Conclusions

The large size and high degree of degeneracy of Rydberg atoms leads to a number of interesting effects that govern their behavior in optical lattices. In this paper, the adiabatic potential surfaces for Rydberg states in a ponderomotive optical lattice have been calculated. The structure of the potentials can be modeled via an effective electric field near the lattice inflection points and an effective magnetic field near the lattice nodes and anti-nodes. For high m_j values, the n-range over which the models are applicable is increased due to a reduction of the extent of the Rydberg atom wavefunction along the lattice laser beam direction. We have demonstrated how the perturbation at the anti-nodes of the lattice electric field resembles the diamagnetic problem and gives rise to rotational and vibrational energy levels. We have shown the adiabatic wavefunctions for some representative cases.

The adiabatic potentials calculated in this paper could be measured spectroscopcally in a ponderomotive optical lattice that is sufficiently deep, such that the individual potentials can be selectively excited. An important question then is whether the photo-ionization rate of a Rydberg atom in a ponderomotive optical lattice is low enough for any of the structures discussed in this paper to be observable. Since both the photo-ionization rate and the lattice depth are proportional to intensity, the significance of photo-ionization can be expressed with a dimensionless factor that scales with the photo-ionization-induced level width divided by the potential depth. This quantity is given by $\chi = \sigma (2c\epsilon_0 m\omega/e^2)$, where σ is the photo-ionization cross-section. For low-angular-momentum states near $n = 50$ and $\lambda = 1064$ nm, we have numerically estimated $\chi \sim 10^{-3}$. Further, we have found that χ approximately scales as n^{-3}, reflecting the fact that photo-ionization occurs near the nucleus of the atom. Also, for higher-angular-momentum states, the photo-ionization cross-section quickly drops and approaches the Thomson cross-section.

Noting that meaningful experiments will only require values of χ of approximately 10^{-2} or less, we are fairly certain that photo-ionization will not present a problem. Preliminary results of ongoing experiments indeed show that there is no indication that photo-ionization of Rydberg atoms due to the lattice light plays a significant role. In these experiments, a ponderomotive optical lattice is formed using two narrowly focused, counter-propagating YAG laser beams. In the future, one could generate a much deeper lattice using a field enhancement cavity centered around the excitation region. Using a resonant two-photon excitation scheme and exploiting the light shifts of the ground and intermediate levels, it is possible to excite Rydberg atoms at well-defined z-positions in the lattices discussed in the present paper. In this way, the accuracy of the effective field models as well as the similarity to the diamagnetic problem could be proven experimentally. Eventually, adiabatic potentials similar to those presented in this paper could be used in applications that require Rydberg atom trapping, such as quantum information processing schemes and high-precision measurements of atomic constants.

IOP Institute of Physics **Φ** DEUTSCHE PHYSIKALISCHE GESELLSCHAFT

Acknowledgments

Appendix. Numerical methods

The following analysis is similar to the theoretical outline found in [10] with the fine structure of the Rydberg atom now taken into account to include all possible state mixing. The lattice potential can be expanded in a Taylor series about $z = 0$:

$$1 + \cos\left(2k\left(z + z_0\right)\right) = \sum_{p=0}^{\infty} K_p z^p, \tag{A.1}$$

where the coefficients K_p are given by

$$K_p = \frac{(2k)^p}{p!} \begin{cases} (-1)^{p/2} \cos\left(2kz_0\right) + \delta_{p,0}, & p \text{ even}, \\ (-1)^{(p+1)/2} \sin\left(2kz_0\right), & p \text{ odd}, \end{cases} \tag{A.2}$$

where $\delta_{p,0}$ is a Kronecker-delta.

In the bound energy range of the Rydberg atom, the Hamiltonian including fine structure can be represented in the basis $\{|n, l, j, m_j\rangle\}$ as

$$H_{n,l,j,m_j}^{n',l',j',m_j'} = E_{n,l,j}\delta_{n,n'}\delta_{l,l'}\delta_{j,j'}\delta_{m_j,m_j'} + \frac{1}{2}V_0\delta_{m_j,m_j'}\sum_{p=0}^{\infty}\left\{K_p\left(r^p\right)_{n,l,j}^{n',l',j'}\right.$$

$$\left. \times \left[C_{l,j,m_j,\uparrow}^* C_{l',j',m_j,\uparrow}\left(\cos^p\theta\right)_{l,m_j-1/2}^{l',m_j-1/2} + C_{l,j,m_j,\downarrow}^* C_{l',j',m_j,\downarrow}\left(\cos^p\theta\right)_{l,m_j+1/2}^{l',m_j+1/2}\right]\right\}, \tag{A.3}$$

where the $E_{n,l,j}$ are the non-perturbed energy levels, and $(r^p)_{n,l,j}^{n',l',j'}$ and $(\cos^p\theta)_{l,m_j\pm1/2}^{l',m_j\pm1/2}$ are the radial and angular matrix elements induced by the optical lattice, respectively. The $C_{l,j,m_j,\uparrow}$ and $C_{l,j,m_j,\downarrow}$ denote the Clebsch–Gordan coefficients for the electron spin in the angular state $|l, j, m_j\rangle$ pointing up or down, respectively. The radial matrix elements, $(r^p)_{n,l,j}^{n',l',j'}$, are calculated numerically using the quantum defects of the atom of interest. The quantization axis for the m_j-quantum number is along the laser beam direction for the ponderomotive optical lattice. Due to the resulting azimuthal symmetry, the magnetic quantum number m_j is conserved. The angular matrix elements can be written as

$$(\cos^p\theta)_{l,m}^{l',m} = (-1)^m\, p! \sum_{\tilde{l}=p,p-2,\ldots,0} \left\{\frac{\left(2\tilde{l}+1\right)\sqrt{(2l+1)\,(2l'+1)}}{2^{(p-\tilde{l})/2}\left(\frac{p-\tilde{l}}{2}\right)!\left(p+\tilde{l}+1\right)!!}\begin{pmatrix}l' & \tilde{l} & l \\ 0 & 0 & 0\end{pmatrix}\begin{pmatrix}l' & \tilde{l} & l \\ -m & 0 & m\end{pmatrix}\right\}$$

$$= (-1)^m\, p!\,\Lambda(l, l', m, p), \tag{A.4}$$

IOP Institute of Physics ⬥ DEUTSCHE PHYSIKALISCHE GESELLSCHAFT

where $m = m_j \pm 1/2$. Using $\Lambda(l, l', m, p)$ as defined in equation (A.4) and after some rearrangement, one finds

$$
H_{n,l,j,m_j}^{n',l',j',m'_j} = E_{n,l,j}\delta_{n,n'}\delta_{l,l'}\delta_{j,j'}\delta_{m_j,m'_j} + \frac{1}{2}V_0\delta_{m_j,m'_j}(-1)^{m_j-1/2+(\tilde{l}_{\min}+\eta)/2}
$$
$$
\times \sum_{p=\tilde{l}_{\min},\tilde{l}_{\min+2},\dots} \left\{ (-1)^{(p-\tilde{l}_{\min})/2}(2k)^p (r^p)_{n,l,j}^{n',l',j'} \left[\cos\left(2kz_0 - \frac{\eta\pi}{2}\right) + \delta_{p,0} \right] \right.
$$
$$
\left. \times \left[C_{l,j,m_j,\uparrow}^* C_{l',j',m_j,\uparrow}\Lambda(l, l', p, m_j - 1/2) - C_{l,j,m_j,\downarrow}^* C_{l',j',m_j,\downarrow}\Lambda(l, l', p, m_j + 1/2) \right] \right\}.
$$
(A.5)

Here, the value $\tilde{l}_{\min} = |l - l'|$ and $\eta = 0$ or 1 for even and odd $\tilde{l}_{\min}$, respectively. Once the Hamiltonian is obtained, the eigenvalues and adiabatic potentials are determined as described in the introduction.

References

[1] Jessen P S and Deutsch I H 1996 *Adv. At. Mol. Phys.* **37** 95
[2] Schneider U, Hackermüller L, Will S, Best Th, Block I, Costi T A, Helmes R W, Rasch D and Rosch A 2008 *Science* **322** 1520–5
[3] Chandrashekar C M and Laflamme R 2008 *Phys. Rev.* A **78** 022314
[4] Ferris A J, Oldsen M K and Davis M J 2009 *Phys. Rev.* A **79** 043634
[5] Dutta S K, Guest J R, Feldbaum D, Walz-Flannigan A and Raithel G 2000 *Phys. Rev. Lett.* **85** 5551–4
[6] Protsenko I E, Reymond G, Schlosser N and Grangier P 2002 *Phys. Rev.* A **65** 052301
[7] Jaksch D, Cirac J I, Zoller P, Rolston S L, Côté R and Lukin M D 2000 *Phys. Rev. Lett.* **85** 2208
[8] Lukin M D, Fleischhauer M, Côté R, Duan L M, Jaksch D, Cirac J I and Zoller P 2001 *Phys. Rev. Lett.* **87** 037901
[9] Choi J H, Knuffman B, Cubel-Liebisch T, Reinhard A and Raithel G 2007 *Adv. At. Mol. Opt. Phys.* **54** 132
[10] Knuffman B and Raithel G 2007 *Phys. Rev.* A **75** 053401
[11] Friedrich S H 2004 *Theoretical Atomic Physics* (Berlin: Springer)
[12] Freeman R R, Buchsbaum P H, Milchberg H, Darack S, Schumacher D and Geusic M E 1987 *Phys. Rev. Lett.* **59** 1092–5
[13] Bucksbaum P H, Schumacher D W and Bashkansky M 1988 *Phys. Rev. Lett.* **61** 1182
[14] Normand D, Lompré L-A, L'Huillier A, Morellec J, Ferray M, Lavancier J, Mainfray G and Manus C 1989 *J. Opt. Soc. Am.* B **6** 1513
[15] O'brian T R, Kim J-B, Lan G, McIlrath T J and Lucatorto T B 1994 *Phys. Rev.* A **49** R649–52
[16] Hertlein M P, Bucksbaum P H and Muller H G 1997 *J. Phys. B: At. Mol. Phys.* **30** 197–205
[17] Paulus G G, Grasbon F, Walther H, Kopold R and Becker W 2001 *Phys. Rev.* A **64** 021401
[18] Afrousheh K, Bohlouli-Zanjani P, Petrus J A and Martin J D D 2006 *Phys. Rev.* A **74** 062712
[19] Zimmerman M L, Castro J C and Kleppner D 1978 *Phys. Rev. Lett.* **40** 1083
[20] Gay J C and Delande D 1983 *Comments At. Mol. Phys.* **13** 275
[21] Cacciani P, Luc-Koenig E, Pinard J, Thomas C and Liberman S 1986 *Phys. Rev. Lett* **56** 1124
[22] van der Veldt T, Vassen W and Hogervorst W 1993 *J. Phys. B: At. Mol. Opt. Phys.* **26** 1945–55
[23] Solov'ev A E 1982 *Eksp. Teor. Fiz* **82** 1762
[24] Cacciani P, Liberman S, Luc-Koenif E, Pinard J and Thomas C 1988 *J. Phys. B: At. Mol. Opt. Phys.* **21** 3475